Plant Science 362 (2026) 112768

Contents lists available at ScienceDirect

Plant Science

journal homepage: www.elsevier.com/locate/plantsci

Research Article

Molecular and structural basis for nitrosoglutathione-dependent redox regulation of triosephosphate isomerase from *Chlamydomonas reinhardtii*

Maria Meloni [a], Edoardo Jun Mattioli [b,c], Silvia Fanti [b], Ginevra Marie Eloise Peppi [a], Tancredi Bin [a], Giuseppe Gabellini [b], Daniele Tedesco [d], Julien Henri [e,f], Paolo Trost [a], Stéphane D. Lemaire [e,f,g], Matteo Calvaresi [b,c,*], Simona Fermani [b,h,**], Mirko Zaffagnini [a,***]

[a] Department of Pharmacy and Biotechnology, University of Bologna, via Irnerio 42, Bologna I-40126, Italy
[b] Department of Chemistry 'G. Ciamician', University of Bologna, via Selmi 2, Bologna I-40126, Italy
[c] IRCCS Azienda Ospedaliero-Universitaria di Bologna, Preclinical & Translational Research in Oncology lab (PRO), Italy
[d] Institute for Organic Synthesis and Photoreactivity (ISOF), National Research Council of Italy (CNR), Bologna I-40129, Italy
[e] Sorbonne Université, CNRS, Department of Computational, Quantitative and Synthetic Biology, Paris F-75005, France
[f] Sorbonne Université, CNRS, INSERM, Institut de Biologie Paris-Seine, Paris F-75005, France
[g] Sorbonne Université, Université de Technologie de Compiègne, CNRS, INSERM, Biofoundry Alliance Sorbonne Université, Paris F-75005, France
[h] Interdepartmental Centre for Industrial Research Health Sciences & Technologies, University of Bologna, Bologna 40064, Italy

ARTICLE INFO

Keywords:
Cysteine thiol
Docking
Nitrosoglutathione
Nitrosothiols
S-nitrosylation
Crystal structure

ABSTRACT

Protein *S*-nitrosylation is a reversible redox-based post-translational modification that plays an important role in cell signaling by modulating protein function and stability. At the molecular level, *S*-nitrosylation consists of the formation of a nitrosothiol (-SNO) and is primarily induced by the trans-nitrosylating agent nitrosoglutathione (GSNO). Triosephosphate isomerase (TPI), which catalyzes the interconversion of dihydroxyacetone phosphate and glyceraldehyde-3-phosphate, has been identified as a putative target of *S*-nitrosylation in both plant and non-plant systems. Here we investigate the molecular basis for GSNO-dependent regulation of chloroplast TPI from the model green alga *Chlamydomonas reinhardtii* (CrTPI). Molecular modelling identified Cys14 and Cys219 as potential sites for interaction with GSNO, though crystallography of GSNO-treated CrTPI revealed *S*-nitrosylation only at Cys14. To disclose GSNO target sites, we generated and characterized Cys-to-Ser variants for Cys14 and Cys219, identifying Cys219 as a key residue mediating the GSNO-dependent modulation of CrTPI activity. Molecular dynamics simulations further revealed the stabilizing interactions of *S*-nitrosylated cysteines with their local environments. Overall, our results indicate that CrTPI catalysis is modulated by GSNO through a redox-based mechanism involving Cys219, which highlights a conserved regulatory strategy shared with human TPI.

1. Introduction

Triose phosphate isomerase (TPI) is a highly conserved enzyme with a central role in carbon metabolism. In plants, TPI participates in the glycolytic/gluconeogenic pathways and photosynthetic carbon fixation *via* the Calvin-Benson-Bassham (CBB) cycle), catalyzing the reversible interconversion of dihydroxyacetone phosphate (DHAP) and glyceraldehyde-3-phosphate (G3P). The enzyme does not require any cofactors and confers a remarkable catalytic efficiency, with a rate enhancement of 10^6-10^9-fold compared to the nonenzymatic reaction (Wierenga et al., 2010; Helliwell, 2021). The catalytic properties of TPI isoforms from both plant and non-plant organisms rely on a conserved structural architecture comprising a TIM-barrel fold and a catalytic tetrad involving an asparagine (Asn), a lysine (Lys), a histidine (His),

Abbreviations: CBB, Calvin-Benson-Bassham; CD, circular dichroism; Cys, cysteine; DHAP, dihydroxyacetone phosphate; DLS, dynamic light scattering; DTNB, 5,5'-dithiobis-2-nitrobenzoic acid; DTT, dithiothreitol; G3P, glyceraldehyde-3-phosphate; GSNO, nitrosoglutathione; NO, nitric oxide; RMSD, root mean square deviation; -SNOs, nitrosothiols; TPI, triose phosphate isomerase.

* Corresponding authors at: IRCCS Azienda Ospedaliero-Universitaria di Bologna, Preclinical & Translational Research in Oncology lab (PRO), Italy.
** Corresponding authors at: Interdepartmental Centre for Industrial Research Health Sciences & Technologies, University of Bologna, Bologna 40064, Italy.
*** Corresponding author.
E-mail addresses: matteo.calvaresi3@unibo.it (M. Calvaresi), simona.fermani@unibo.it (S. Fermani), mirko.zaffagnini3@unibo.it (M. Zaffagnini).

https://doi.org/10.1016/j.plantsci.2025.112768
Received 13 May 2025; Received in revised form 29 July 2025; Accepted 10 September 2025
Available online 12 September 2025

and a glutamate (Glu) (Asn12, Lys14, His96, and Glu166 in human TPI). The catalytic residues participate in the isomerization reaction by stabilizing the substrate (Asn and Lys) or by acting as general acid/base that facilitates the proton transfer required for catalysis (His and Glu) (Wierenga et al., 2010; Helliwell, 2021). Considering its dual metabolic role, in most eukaryotic phototrophs two genes code for the glycolytic and photosynthetic isoforms. In this regard, the unicellular green alga *Chlamydomonas reinhardtii* is an exception, as it possesses only a single gene encoding TPI (Zaffagnini et al., 2014). This peculiar situation is explained by the fact that in this microalga the portion of the glycolytic pathway involving TPI takes place in the chloroplast rather than in the cytosol (Johnson and Alric, 2013). A previous biochemical study on TPI from *Chlamydomonas reinhardtii* (CrTPI) revealed that this enzyme shares similar catalytic properties (*i.e.*, kinetic parameters) with glycolytic isoforms of heterotrophic and autotrophic organisms, but possesses a catalytic proficiency higher than the photosynthetic isoforms from land plants (Zaffagnini et al., 2014).

In cellular systems, metabolic fluxes are controlled through regulatory mechanisms operating at the molecular level, mainly through modulation of enzyme activities. In this context, redox modifications of cysteines act as regulatory molecular switches in response to physiological or stress stimuli (Zaffagnini et al., 2012, 2019a). Among redox modifications, *S*-nitrosylation, which consists of the formation of nitrosothiols (-SNOs) between protein cysteines and nitric oxide (NO), plays a central role in the regulation of protein function and structural stability (Hess et al., 2005; Foster et al., 2009; Zaffagnini et al., 2016). Over the past decades, numerous proteomics-based studies have identified hundreds of putative *S*-nitrosylation targets, including several CBB cycle enzymes (Lindermayr et al., 2005; Shi et al., 2008; Tanou et al., 2009; Lin et al., 2012; Tanou et al., 2012; Morisse et al., 2014b; Zahid et al., 2014; Hu et al., 2015; Qiu et al., 2019). Among these, TPI isoforms from both plant and non-plant sources have been detected, highlighting the potential role of this redox modification in modulating carbon metabolism under stress conditions associated with disrupted GSNO homeostasis (Michelet et al., 2013; Morisse et al., 2014b; Chen et al., 2016). Despite extensive proteomic evidence, functional characterization of *S*-nitrosylation-dependent regulation of TPI activity has thus far been established only for the *Chlamydomonas reinhardtii* and human (HsTPI) isoforms (Zaffagnini et al., 2014; Romero et al., 2018). The occurrence of *S*-nitrosylation and its effect on catalysis were ascertained for both enzymes *in vitro*, but the identification of cysteine site(s) and molecular mechanisms underlying *S*-nitrosylation have been solely investigated for HsTPI.

To elucidate the molecular bases that underpin the redox control of CrTPI exerted by *S*-nitrosylation, we combined computational modeling with structural and functional studies to identify the cysteine residues targeted by nitrosoglutathione (GSNO), a major physiological *S*-nitrosylating agent. Additionally, we generated Cys-to-Ser mutants at key positions (C14S and C219S) to assess their impact on catalytic function and GSNO sensitivity. Our findings provide mechanistic insights into the significance of GSNO-dependent redox regulation of CrTPI, which highlights a prominent role of Cys219 in this process. In addition, understanding this regulatory mechanism will broaden our knowledge of how redox-based modulation influences carbon metabolism in the model green alga *Chlamydomonas reinhardtii*. This insight may reveal how redox signals integrate with metabolic pathways to fine-tune photosynthetic efficiency and carbon flux under varying environmental conditions.

2. Material and methods

2.1. Material

PD-10 and NAP-5 columns were obtained from Cytiva Life Science. GSNO (nitrosoglutathione) was freshly prepared as described in Treffon et al. (2021). All other chemicals and enzymes were obtained from Merck Life Science unless otherwise specified.

2.2. Site-directed mutagenesis

The two cysteine residues in CrTPI at positions 14 and 219 were mutated into serines by PCR site-directed mutagenesis using the pET-3c/CrTPI as a template (Zaffagnini et al., 2014) The mutagenic pairs of primers (Table S1) were used according to the procedures of the QuikChange site-directed mutagenesis kit (Stratagene). All mutations were confirmed by DNA sequencing.

2.3. Protein purification

Recombinant CrTPI (WT and Cys mutants) was produced using the pET-3c-His/BL21 expression system as described previously with minor modifications (Zaffagnini et al., 2014). Bacteria were grown at 37 °C in LB medium supplemented with 100 μg/ml ampicillin, and protein production was induced with 0.2 mM isopropyl-β-D-thiogalactopyranoside at 37 °C for 3 h. Cells were then harvested by centrifugation and resuspended in 30 mM Tris-HCl (pH 7.9) (buffer A). Cell lysis was performed using a combination of lysozyme (100 μg per ml of cell suspension) and sonication (5 cycles of 2 min each) (Meloni et al., 2024b). Cell debris were removed by centrifugation (15 000 *x* g for 45 min) and the supernatant was applied onto a Ni^{2+}-Hitrap chelating resin (HIS--Select Nickel Affinity Gel) equilibrated with buffer A containing 500 mM NaCl and 5 mM imidazole. After extensive washing with buffer A supplemented with 30 mM imidazole, the recombinant protein was eluted from the column by using buffer A containing 250 mM imidazole. Eluted fractions were immediately desalted using PD-10 equilibrated with buffer A supplemented with 1 mM EDTA. The molecular mass and purity of the protein were analyzed by SDS-PAGE, and the concentration of purified CrTPI forms was determined spectrophotometrically using a molar extinction coefficient at 280 nm of 37,930 M^{-1} cm^{-1}.

2.4. Gel filtration and dynamic light scattering analysis of CrTPI

Before gel filtration analysis, CrTPI WT and Cys mutants (C14S and C219S) were treated with 20 mM reduced dithiothreitol (DTT) for 1 h at room temperature. Analytical gel filtration profiles of reduced CrTPI forms were performed on a Superdex 200 10/300 GL column (Cytiva Life Sciences) connected to an ÅKTA Purifier system (Cytiva Life Sciences). The column was calibrated with standard proteins as described in (Tagliani et al., 2021). The protein was eluted at a flow rate of 0.5 ml min^{-1} with 50 mM Tris-HCl (pH 7.5) containing 150 mM KCl. For each recombinant CrTPI form, fractions containing pure proteins were collected, concentrated, desalted with NAP-5 columns equilibrated with buffer A supplemented with 1 mM EDTA, and used for further biochemical analyses. Dynamic light scattering measurements of CrTPI WT and Cys mutants were carried out as in Zaffagnini et al. (2019b). Briefly, protein solutions (10 mg ml^{-1}) were incubated in buffer A containing 0.5 mM EDTA. The size distribution of the particles in solution and their hydrodynamic radius were measured. The data were obtained using Zetasizer Nano (Malvern) cuvettes, and 10 spectra were acquired for each DLS analysis. The above data were then averaged and used to determine the hydrodynamic diameter and polydispersity using the average autocorrelation function.

2.5. Determination of free sulfhydryl groups in CrTPI WT and Cys mutants

The number of free thiols in CrTPI WT and Cys mutants (C14S and C219S) was determined spectrophotometrically under non-denaturing conditions with 5,5'-dithiobis-2-nitrobenzoic acid (DTNB) (Meloni et al., 2024a). Briefly, 10 μM protein was incubated for 30 min with 20 mM dithiothreitol (DTT) and then desalted with PD-10 equilibrated with buffer A. Subsequently, the pre-reduced protein was added to a

solution containing 0.2 mM DTNB in 100 mM Tris–HCl (pH 7.9), and after 30 min at room temperature, the absorbance at 412 nm was determined spectrophotometrically using a Cary 60 UV-Vis spectrophotometer (Agilent Technologies). A molar extinction coefficient of 14, 150 M^{-1} cm^{-1} was used to calculate the number of titrated sulfhydryl groups (Morisse et al., 2014a).

2.6. Circular dichroism spectroscopy

Samples of CrTPI WT and Cys mutants (15 μM) were prepared in 50 mM Tris-HCl buffer (pH 7.5) containing 150 mM KCl, and quantified by spectrophotometric analysis at 280 nm in a 1 cm cell (ε_{280} = 37,930 M^{-1} cm^{-1}). Far-UV circular dichroism (CD) spectra (250–195 nm) were measured at room temperature on a J-715 spectropolarimeter (Jasco, Japan), using a QS-quartz cylindrical cell with 0.2 mm optical pathlength (Hellma Analytics, Germany), a 2 nm spectral bandwidth, a 50 nm/min scanning speed, a 2 s data integration time, a 0.5 nm data interval, and an accumulation cycle of 3 scans per spectrum. The resulting CD spectra were blank-corrected and converted to molar units per residue ($\Delta\varepsilon_{res}$, in M^{-1} cm^{-1}).

2.7. Activity assay

The catalytic activity of recombinant CrTPI forms was measured spectrophotometrically as described in Zaffagnini et al. (2014). Briefly, the reaction was measured in the G3P to DHAP direction in an assay mixture containing 100 mM triethanolamine (pH 7.4), 10 mM EDTA, 0.01 % bovine serum albumin, 2 mM G3P, 2 units ml^{-1} of *S. cerevisiae* α-glycerophosphate dehydrogenase (α-GDH), and 0.2 mM NADH. The reaction was initiated by adding CrTPI and its activity was calculated from the decrease in absorbance at 340 nm (*i.e.* NADH oxidation).

2.8. Treatments of CrTPI WT and Cys mutants with thiol-modifying agents

Inactivation treatments were performed at room temperature by incubating CrTPI (WT and Cys mutants) in 100 mM Tris-HCl (pH 7.9) with 0.2 mM DTNB or 1 mM GSNO. At the indicated times (15, 30, and 60 min), an aliquot of incubation mixtures was withdrawn in order to evaluate enzyme activity monitored as described above.

2.9. Crystallization and data collection

Prior crystallization trials, purified CrTPI WT and Cys mutants (C14S and C219S) were incubated in buffer A in the absence (untreated) or presence of 2 mM GSNO (GSNO-treated). Subsequently, protein samples were concentrated to 10 mg ml^{-1} in buffer A containing 0.5 mM EDTA and crystallized by hanging drop vapor-diffusion method at 293 K. Aliquots of 2 μl were then mixed with an equal volume of reservoir solution and the final drop was equilibrated against 700 μl of reservoir solution. CrTPI and GSNO-treated CrTPI crystals were obtained in 0.1 M Hepes-NaOH (pH 7.5) using 50 % and 55 % v/v MPD, respectively. For C14S mutant, a reservoir solution containing 0.1 M Bis-Tris (pH 5.0) and 17.5 % w/v PEG 3350 was used. When present, crystals appeared as a rectangular prism in case of CrTPI WT (untreated and GSNO-treated) or needle-like in case of the C14S mutant. No crystals were obtained for both C219S (untreated and GSNO-treated) and C14S mutants (GSNO-treated). Some crystals from untreated CrTPI samples (WT and C14S mutant) were soaked in the reservoir solution containing 2 mM of GSNO for 120 min. Crystals of C14S mutant dissolved during soaking.

Crystals of GSNO-soaked and GSNO-treated CrTPI WT were directly frozen in liquid nitrogen, while crystals of CrTPI-C14S were soaked into a cryo-protectant solution containing 20 % w/v PEG 3350 and 20 % v/v PEG 200. Diffraction data for crystals of CrTPI WT (GSNO-treated) and C14S mutant were collected at 100 K at the European Synchrotron Radiation Facility (Grenoble, beamline ID30A-3), while those of GSNO-soaked CrTPI were collected at Diamond Light Source (Oxford, beamline I03). Data were collected at a resolution of 1.2 Å for GSNO-soaked CrTPI, 1.55 Å for GSNO-treated CrTPI, and 3.55 Å for CrTPI-C14S, and then processed using the beamline pipeline XIA2 DIALS (Gildea et al., 2022) and AUTOPROC (Vonrhein et al., 2011) and then scaled with AIMLESS (Evans and Murshudov, 2013). The correct space group was determined by POINTLESS (Evans, 2006) and confirmed in the structure solution stage. Data collection parameters and statistics are reported in Table S2.

2.10. Structure solution and refinement

CrTPI structures were solved by molecular replacement using the program PHASER (McCoy et al., 2007) from the CCP4 package (Winn et al., 2011) using the structure of CrTPI (PDB ID: 4MKN; (Zaffagnini et al., 2014) excluding non-protein atoms and water molecules, as a search model. The refinement was performed with REFMAC5 7.1.004 (Murshudov et al., 1997) from the CCP4 package (Winn et al., 2011), selecting 5 % of reflection for R_{free}. The molecular graphic software COOT (Emsley and Cowtan, 2004) was used for manual rebuilding and modelling. Water molecules were automatically added and, after a visual inspection, confirmed in the model if the relative electron density value in the (2*Fo* – *Fc*) maps exceeded 0.19 e-$Å^{-3}$ (1.0 σ) and if they fell into an appropriate hydrogen bonding environment. Inspection of the Fourier difference maps of GSNO-soaked CrTPI crystals, showed an extra electron density close to the thiol group of Cys14 that was attributed to the NO group bound to the sulfur. Therefore, an *S*-nitrosylated cysteine was inserted into the model with an occupation of 0.67. The last refinement cycle was performed with PHENIX.REFINE (Adams et al., 2010) from the PHENIX suite (Liebschner et al., 2019). Figures were generated using Pymol (The PyMOL Molecular Graphics System, Version 1.2r3pre, Schrödinger, LLC). Final refinement statistics are reported in Table S2.

2.11. Computational analysis for docking of GSNO with CrTPI

To identify the most probable interaction sites between GSNO and CrTPI a molecular docking study was carried out using the program AutoDock VINA (Trott and Olson, 2010). CrTPI structure (PDB: 4MKN) was prepared for docking by removing water, organic molecules, and ions. Protons were added using the H++ websever setting a pH equal to 7.4 (Anandakrishnan et al., 2012). The grid for the docking was centered in each available cysteine of the CrTPI structure.

2.12. Molecular mechanics calculations

The best docking poses were used to generate the initial coordinates for molecular mechanics (MM) calculations. MM calculations were performed using the AMBER 22 package (Case et al., 2005). The FF14SB force field (Maier et al., 2015) was used to model CrTPI. Parameters for GSNO developed in Mattioli et al. (2022) were used. 2500 steps of steepest descent minimization, followed by additional 2500 steps of conjugate gradient minimization were performed with the "Sander" module of Amber (Case et al., 2005). The minimized structures were used to estimate the interaction energy between GSNO and CrTPI using the MM-generalized Born surface area (MM-GBSA) protocol (Kollman et al., 2000).

Molecular dynamic (MD) simulations of the WT and *S*-nitrosylated CrTPI proteins were carried out using the Particle Mesh Ewald summation (with cut off radius of 10.0 Å). H-atoms were considered by the SHAKE algorithm, and a time step of 2 fs was applied in all MD runs. For the *S*-nitrosylated cysteine an *ad hoc* force field developed by Han was used (Han, 2008). All simulations were performed with explicit solvent by using the TIP3P water model. Starting from the CrTPI structure and the corresponding *S*-nitrosylated forms, 500 steps of steepest descent minimization, followed by additional 9500 steps of conjugate gradient

minimization were performed with PMEMD (Case et al., 2005). To equilibrate the systems, 1 ns of heating to 298 K within an NPT ensemble and temperature coupling according to Langevin was used. Production runs of 100 ns were carried out. Trajectories obtained from the MD simulations were post-processed using CPPTRAJ (Case et al., 2005). One snapshot each 0.1 ns was extracted from the calculated MD trajectories to estimate the contributions to the binding of the single amino acids of CrTPI with Cys-SH and Cys-SNO (decomposition analysis), using the MM-GBSA approach (Kollman et al., 2000).

2.13. Replicates and statistical analyses

All the experimental results reported are representative of at least 3 independent biological replicates and expressed as mean ± SD. Statistical analysis was performed using an unpaired *t*-test with Welch's correction in the case of two categories or two-way ANOVA followed by a Tukey's post hoc test for multiple comparisons. Letters were used to distinguish groups that differ significantly, as indicated in the figure legends. Asterisks were used to indicate *P*-values ($^{*}P \leq 0.05$, $^{**}P \leq 0.01$, $^{***}P \leq 0.001$, $^{****}P \leq 0.0001$).

2.14. Accession numbers

The atomic coordinates and structure factors of GSNO-soaked CrTPI and CrTPI-C14S structures have been deposited in Protein Data Bank with the accession number 9QM7, 9R6M, respectively. The coordinates of GSNO-treated CrTPI were not deposited since the structure of the WT protein was already present in the data bank.

3. Results and discussion

3.1. Conservation, accessibility, and reactivity of cysteine residues in TPI from Chlamydomonas reinhardtii

CrTPI is a homodimer that contains five cysteine residues per subunit (Cys14, Cys126, Cys194, Cys219, and Cys247) (Fig. 1a and b), none of which is directly involved in the catalytic cycle (Zaffagnini et al., 2014). A comparative analysis of cysteine residue conservation between CrTPI and HsTPI (*i.e.*, TPI isoforms showing sensitivity to *S*-nitrosylation (Zaffagnini et al., 2014; Romero et al., 2018)) revealed that only Cys126 (Cys126 in HsTPI) and Cys219 (Cys217 in HsTPI) are conserved (Fig. 1a-c). Cys126 is widely conserved across most organisms, while Cys219 is not conserved in chloroplast TPIs of land plants but is present in cytoplasmic isoforms of plant origin and in those of mammalian cells and certain endoparasites (Zaffagnini et al., 2014). The remaining cysteines of CrTPI (Cys14, Cys194, and Cys247) are found either in oxygenic phototrophs, heterotrophic prokaryotes and eukaryotes, and endoparasites (Cys14), or are uniquely conserved in green algae (Cys194 and Cys247) (Zaffagnini et al., 2014).

Solvent accessibility of CrTPI cysteines was previously determined by analyzing the three-dimensional structure of native CrTPI (*i.e.*, dimeric conformation; PDB ID: 4MKN) (Zaffagnini et al., 2014). In this protein conformation, Cys219 appeared as the sole cysteine exposed to the solvent, while all remaining cysteine residues showed low or no accessibility. To investigate whether this structural observation correlates with the reactivity of thiol groups, we quantified the number of free thiols in native dimeric reduced CrTPI using the chromogenic Ellman's reagent (5,5′-dithiobis-(2-nitrobenzoic acid), DTNB) following treatment with reducing agents. In contrast with structural predictions, we found that pre-reduced CrTPI contains ~4 cysteine thiols reactive towards DTNB (4.14 ± 0.12). The discrepancy between crystal structure-based solvent accessibility and DTNB-dependent thiol titration as measured in solution may reflect the intrinsic flexibility of the protein backbone or the Cys side chains in solution. Such dynamic conformational changes could transiently expose otherwise buried thiol groups, rendering them chemically reactive.

3.2. Docking analysis reveals that GSNO can potentially interact with two CrTPI sites located in proximity of Cys14 and Cys219

At the physiological level, nitrosoglutathione (GSNO) is considered the main bioactive form of NO, acting as a trans-nitrosylating agent of protein cysteines. GSNO interaction with a cysteine residue requires not only thiol accessibility, but also a favorable local microenvironment that enhances thiol reactivity, particularly by promoting thiol deprotonation to the more nucleophilic thiolate ($-S^-$) form, and supports stable binding of the oxidizing molecule (Mattioli et al., 2022). To investigate potential *S*-nitrosylation sites in CrTPI, we carried out a docking analysis using the structural coordinates of the native enzyme (PDB ID 4MKN; (Zaffagnini et al., 2014) to identify favorable GSNO binding sites (Fig. 2). Given the dimeric structure of CrTPI, Cys219 emerged as the preferred site for GSNO binding ($\Delta G_{binding}$ = –16.6 kcal mol^{-1}) (Fig. 2a). This suggests that this residue, besides being solvent exposed, is surrounded by a microenvironment favoring the interaction with GSNO. Since biochemical assays had indicated the presence of four reactive cysteine thiols, docking experiments were repeated using the monomeric form of CrTPI. In this conformation, Cys 14 was found to be solvent-exposed (ASA of 128 Å^2), consistent with previous observations for both glycolytic and photosynthetic TPI isoforms from the model plant *Arabidopsis thaliana* (AtTPIs) (ASA of 129.3 Å^2 and 127.2 Å^2 for Cys13/Cys15 corresponding to Cys14 in CrTPI, respectively) (Lopez-Castillo et al., 2016). Docking analysis revealed that in the monomeric structure of the protein, the binding site of GSNO in the proximity of Cys219 was obviously maintained ($\Delta G_{binding}$ = –16.6 kcal mol^{-1}), but a second GSNO binding site, close to Cys14 and less accessible in the dimer, appears preferred ($\Delta G_{binding}$ = –18.4 kcal mol^{-1}) (Fig. 2b).

3.3. Crystal structure of S-nitrosylated CrTPI reveals the presence of a nitrosothiol at Cys14

After determining possible GSNO-binding cysteine residues, we analyzed the structural consequences of *S*-nitrosylation by determining the crystal structure of CrTPI treated with GSNO in solution (hereafter GSNO-treated CrTPI) or *in crystallo* (CrTPI crystals treated with GSNO; hereafter GSNO-soaked CrTPI). The 3D-structures of GSNO-soaked and GSNO-treated CrTPI were obtained and solved at 1.20 Å and 1.55 Å resolution, respectively. As with the native structure, the asymmetric units of both structures contain one monomer that shows the typical $(\beta/\alpha)_8$-barrel fold (Figure S1a) (Banner et al., 1975) and forms a homodimer by a two-fold crystallographic axis (Figure S1b). By inspecting the electron density maps, we observed no difference between native and GSNO-treated CrTPI, indicating that exposure to the trans-nitrosylating agent did not induce any stable redox modification of cysteine residues. Indeed, we have to consider that nitrosothiols form inherently labile covalent bonds and X-ray irradiation can speed up their degradation.

In contrast, GSNO-soaked CrTPI showed an extra electron density near Cys14 side chain, which was attributed to the presence of a covalently bound nitrosothiol group(-SNO) (Fig. 3a). Refinement of GSNO-soaked CrTPI revealed that Cys14-SNO has a dual conformation (conformation 1 and 2), with one of the two being more populated than the other (q=0.67) (Fig. 3b).

As depicted in Figure S1b, Cys14 is located at the dimer interface, within a loop between strand β1 and helix α1 which also includes the catalytic residues Asn11 and Lys13. *S*-nitrosylation of Cys14 did not induce a global conformation change, as evidenced by the root mean square deviation (RMSD) of 0.29 Å for the superposition of C_α atoms of WT and GSNO-soaked CrTPI structure. In the most populated conformation (conformation 1), the nitrosothiol is inserted into a hydrophobic cavity defined by residues from the adjacent subunit (Trp67, Phe74, the aliphatic chain of Glu77 and Val78) and forms a π-staking interaction with Trp67 (Fig. 3c). Additional stabilization is provided by three hydrogen bonds with the main chain amino group of Val78 and Ser79

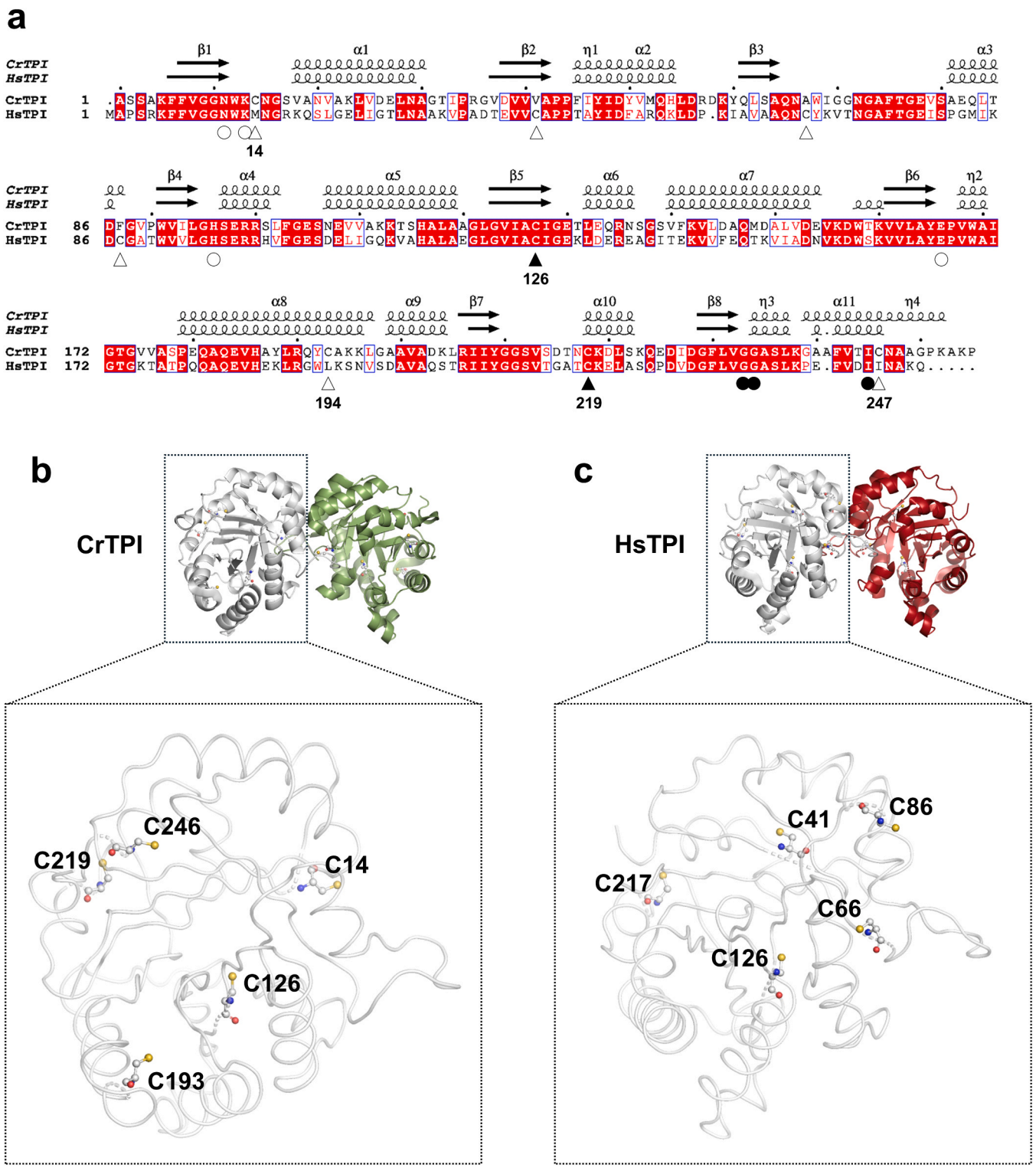

Fig. 1. Comparison of primary sequence and cysteine residues position between CrTPI and HsTPI. (a) Primary and secondary structure alignment of 3D-solved CrTPI and HsTPI. The alignment was performed with Espript (http://espript.ibcp.fr) (Gouet et al., 1999) using the sequence and the structure of TPI from *Chlamydomonas reinhardtii* (CrTPI, PDB ID: 4MKN; UniProtKB: Q5S7Y5) and TPI from *Homo sapiens* (HsTPI, PDB ID: 2JK2; UniProt: P60174). The conserved residues are shown in red background; blue boxes represent conserved amino acid stretches (>70 %). Residues with similar physico-chemical properties are indicated in red. α-helices, β-strands and 3_{10}-helices are marked with α, β, η respectively. Conserved and non-conserved cysteine residues are indicated by closed and open triangles, respectively. Numbering of cysteine residues in CrTPI is shown. Open circles denote catalytic residues, while closed circles indicated residues likely involved in the direct/indirect interaction with Cys219-SNO and Cys217-SNO in CrTPI and HsTPI, respectively. The primary sequence alignment was made using Clustal Omega (Sievers et al., 2011). **(b)** Ribbon representation of CrTPI dimer (top) and cartoon representation of the protein main chain with cysteine residues (bottom). **(c)** Ribbon representation of HsTPI dimer (top) and cartoon representation of the protein main chain with cysteine residues (bottom).

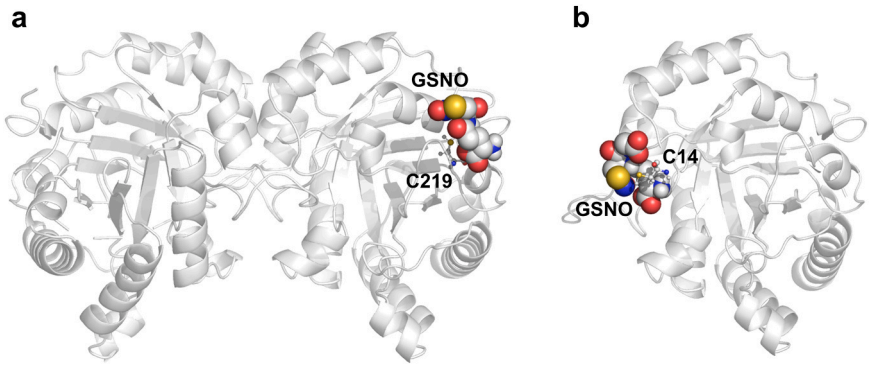

Fig. 2. Crystal structure of CrTPI dimer and monomer highlighting GSNO binding sites. (a) Ribbon representation of the CrTPI dimer with GSNO positioned in the proximity of Cys219. **(b)** Ribbon representation of the CrTPI monomer with GSNO positioned in the proximity of Cys14.

(Fig. 3c). In the minor conformation, the SNO moiety is stabilized by more extensive intra- and inter-chain hydrogen bonds including the main chain amino group of Asn15 and the side chains of Asn71 of the same subunit (Fig. 3d). Moreover, the main chain atoms of Cys14-SNO are hydrogen bonded to the amino and carbonyl groups of Gly72 of the adjacent subunit. All these residues interacting and stabilizing the NO group of the modified Cys14 lie in a long loop (Q64-A80; Fig. 1a) between strand β3 and helix α3, which protrudes toward the active site of the adjacent subunit and concurs to its completion (Figure S1b). On this basis, we can hypothesize that *S*-nitrosylation of Cys14 could alter active site geometry by restricting the conformational flexibility of the loop. This structural limitation is absent in the CrTPI WT as Cys14 forms a single interaction with Ser79 involving its thiol group, besides the conserved interactions with Asn71 and Gly72 involving the atoms of its main chain (Figure S1c).

No evidence of redox modification was detected at Cys219 or any of the other cysteine residues (Cys126, Cys194 and Cys247). The lack of nitrosothiol formation at Cys219 after GSNO treatment is likely due to restricted accessibility of the thiol group, which can be significantly influenced by crystal packing constraints. Indeed, the inspection of the crystal packing of CrTPI WT shows that Cys14 seems more easily reachable through solvent channels than Cys219, which is shielded by a symmetry molecule (Figure S2).

3.4. Functional and structural features of CrTPI mutants lacking Cys14 and Cys219

Based on structural and computational evidence, we identified Cys14 and Cys219 as potential redox-regulatory thiols susceptible to GSNO-dependent modification. To experimentally assess their functional relevance, we produced and purified Cys-to-Ser mutants (C14S and C219S) and compared their functional and structural properties to the WT enzyme. In terms of specific activity, the C219S mutant retained full catalytic efficiency, while the C14S variant was less active, retaining ~80 % of WT activity (Fig. 4). Given that Cys14 lies at the dimer interface (Fig. 1b and Figure S1b), its mutation might destabilize the dimeric formation and impair activity. However, gel filtration analysis revealed that the elution profile of the C14S mutant was identical to that of WT (Figure S3a and S3b), indicating that the mutation of Cys14 does not alter dimer conformation. The same result was obtained for the C219S mutant (Figure S3c). To assess whether the decrease in the activity of C14S may depend on conformational changes related to alterations in secondary structure, we conducted circular dichroism (CD) analysis in the 250–195 nm range. CD spectra revealed no significant differences between the WT and Cys mutants (Figure S4).

Crystals were obtained only for the C14S mutant, but they diffracted at very low resolution (Table S2), likely due to heterogeneity in the protein solution. Despite SEC purification, the C14S mutant displayed an intrinsic tendency to form oligomers as evidenced by dynamic light scattering (DLS) analysis performed on concentrated protein solutions (10 mg ml^{-1}). DLS measurements revealed a hydrodynamic radius of 6.3 ± 1.6 nm for the C14S variant, compared to 3.48 ± 0.2 nm for the WT (*i.e.*, dimeric conformation). The crystal structure of C14S confirmed that the point-mutation does not alter global folding or the dimer interface, and differently from the WT protein, the asymmetric unit contains a whole dimer (subunits A and B). The overall structure was conserved, with RMSD values of 0.81 Å for dimer superposition, and 0.56 Å and 0.54 Å for CrTPI-C14S (subunit A) – CrTPI and CrTPI-C14S (subunit B) – CrTPI monomers superimposition, respectively.

Altogether, these results indicate that the substitution of Cys14 and Cys219 does not perturb the structural integrity of CrTPI. Hence, the mild decrease in the activity of the C14S mutant is likely due to its proximity with the catalytic residues such as Lys13. Moreover, substituting Cys14 with a more hydrophilic Ser increases the number of interchain hydrogen bonds, stiffening the dimer interface (Figure S1d). The residues involved (Gly70, Gly72, Phe74, Glu77, Ser79 and Gln82) belong to the loop of the adjacent subunit between strand β3 and helix α3, which contributes to active site formation. A decreased flexibility of this loop may explain the decreased activity of the C14S mutant.

3.5. Redox response of CrTPI WT and Cys variants to oxidative treatments

After characterizing the functional and structural properties of C14S and C219S, we assessed their redox sensitivity by examining their catalytic response to the thiol-modifying agent DTNB and the trans-nitrosylating agent GSNO. Whereas the reaction of DTNB with cysteine residues is driven primarily by solvent accessibility of thiol groups, the interaction between GSNO and cysteine residues also depends on thiol reactivity and the cysteine local microenvironment (Mattioli et al., 2022). As shown in Fig. 5a and 5b, WT CrTPI and the C14S variant were similarly sensitive to DTNB retaining ~20 % and ~5 % residual activity after incubation for 15 and 30 min, respectively. By contrast, the C219S mutant proved to be less sensitive to DTNB with 60 % inhibition after 30 min treatment (Fig. 5c), indicating that Cys219 contributes significantly to DTNB sensitivity. We then examined the response to GSNO (1 mM) by assaying residual activities at different time points. As previously observed, GSNO caused a 50 % inhibition of WT activity after 30 min, which did not diminish after prolonged incubation (60 min) (Fig. 5d). In contrast, the C14S mutant exhibited a greater sensitivity with 60 % inhibition at 30 min, further decreasing to 80 % by 60 min (Fig. 5e). Strikingly, the C219S mutant completely lost sensitivity to GSNO treatment, showing no significant loss of activity at any time point (Fig. 5f). Taken together, these results indicate that Cys219 is the principle site mediating GSNO-dependent inhibition of CrTPI activity, whereas Cys14 does not seem to play a direct role in this redox regulation. Indeed, C14S showed a stronger inhibition than WT, suggesting that the absence of Cys14 might indirectly influence redox

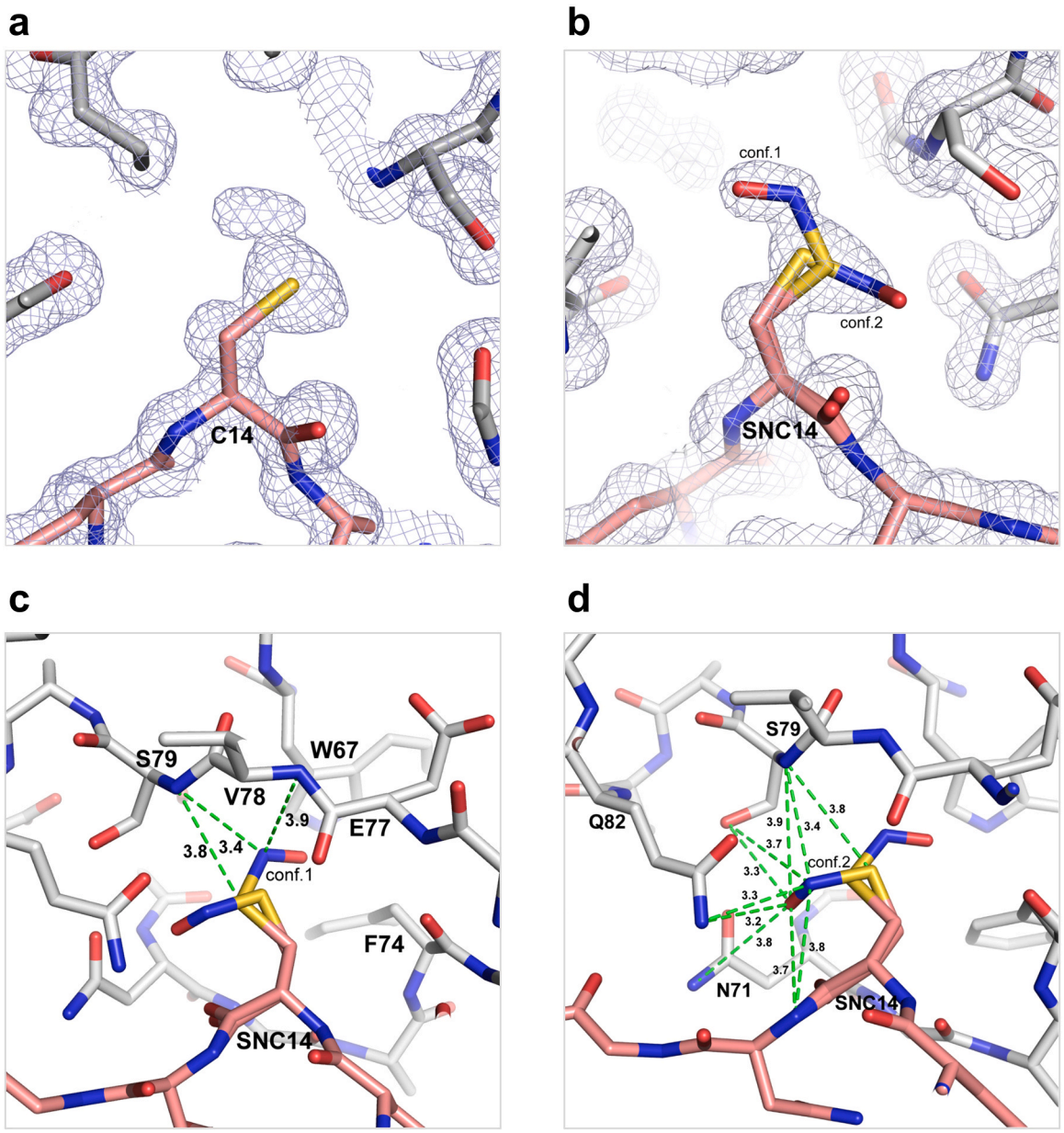

Fig. 3. Electron density and interaction of *S*-nitrosylated Cys14 in CrTPI. **(a)** $2F_o - F_c$ electron density map (contoured at 1.0 σ) showing an extra density at Cys14-SH (C14). **(b)** $2F_o - F_c$ electron density map (contoured at 1.0 σ) of Cys14-SNO (SNC14) highlighting two possible conformations (conf. 1 and 2) of the nitrosothiol (see "results and discussion" for further details). **(c)** Hydrogen bonds (distance ≤4 Å) of Cys14-SNO (SNC14) in the conf. 1 with protein residues. As highlighted in the panel, Cys14-SNO is stabilized by three hydrogen bonds with the main chain amino group of Val78 and Ser79 (SNC14(A) ND – Val78(B) N 3.9 Å; SNC14(A) ND – Ser79(B) N 3.4 Å; SNC14(A) SG – Ser79(B) N 3.6 Å). **(d)** Hydrogen bonds (distance ≤4 Å) of Cys14-SNO in the conf. 2 with protein residues. As highlighted in the panel, the SNO group of Cys14 is stabilized by a higher number of intra- and inter-chain hydrogen bonds involving the main chain amino group of Asn15 (SNC14(A) OE – Asn15(A) N 3.7 Å; SNC14(A) OE – Asn15(A) N 3.8 Å) and Ser79 (SNC14(A) OE – Ser79(B) N 3.9 Å; SNC14(A) ND – Ser79(B) N 3.4 Å; SNC14 (A) SG – Ser79(B) N 3.8 Å), the side chains of Asn71 (SNC14(A) OE – Asn71(B) ND2 3.8 Å), Ser79 (SNC14(A) OE – Ser79(B) OG 3.3 Å; SNC14(A) ND – Ser79(B) OG 3.7 Å), and Gln82 (SNC14(A) OE – Gln82(B) NE2 3.2 Å; SNC14(A) ND – Gln82(B) NE2 3.3 Å). In addition, the main chain atoms of Cys14-SNO are hydrogen bonded to the amino and carbonyl groups of Gly72 of the adjacent subunit (SNC14(A) N – Gly72(B) O 3.0 Å; SNC14(A) O – Gly72(B) N 2.8 Å).

sensitivity.

3.6. *Molecular dynamics calculation to assess the stability and interaction of S-nitrosothiols in CrTPI*

After establishing that Cys219 plays a key role in determining the redox sensitivity of CrTPI to GSNO, we investigated the structural context and stability of its *S*-nitrosylated form (Cys219-SNO) within its microenvironment using molecular dynamics (MD) simulations. The same computational analysis was also conducted for Cys14-SNO, which was experimentally confirmed to undergo *S*-nitrosylation by X-ray crystallography. We carried out per-residue molecular mechanics-generalized Born surface area (MM-GBSA) decomposition analysis of the MD trajectories to calculate the binding energies of cysteine residues in both reduced (-SH) and *S*-nitrosylated (-SNO) forms (Table 1). This analysis showed that the local protein microenvironment more strongly stabilizes the *S*-nitrosylated forms than the corresponding thiols for both Cys14 and Cys219. Notably, Cys14-SNO was stabilized to a greater extent than Cys219-SNO, with binding energy differences of 5.9 kcal mol^{-1} and 2.0 kcal mol^{-1}, respectively (Table 1). The chemical

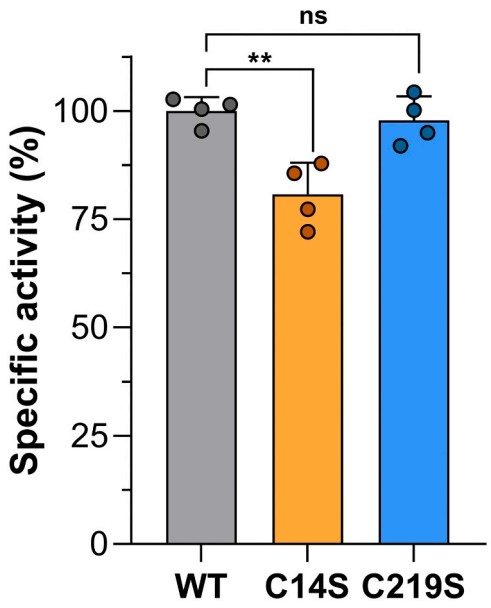

Fig. 4. Specific activities of CrTPI WT and Cys mutants. Activity of recombinant CrTPI WT (gray bar), CrTPI-C14S (C14S, orange bar), and CrTPI-C219S (C219S, light blue bar) was measured as described in "Material and Methods" section. Activity of CrTPI WT (2788.5 ± 89.9 μmol min^{-1} mg^{-1}) was set to 100 % and used to calculate the percentage of C14S and C219S activities (2250.8 ± 203.2 and 2728.6 ± 153.6 μmol min^{-1} mg^{-1}, respectively). Data are represented as mean ± SD (n = 4). Statistical analysis was performed using an unpaired *t*-test and *P* values are reported on graphs as follows: $^{**}P \leq 0.01$, ns: not significant.

origin of the stabilization provided by the various protein residues was then analyzed (Fig. 6). For Cys14-SNO, several residues belonging to both monomers contributed to the stabilization through a network of hydrogen bonds or π-staking interactions involving Trp67, as already identified by crystallographic investigation (Fig. 6a and c). In contrast, the stabilization of Cys219-SNO was limited to only one residue, namely Lys220 that is solvent-exposed in CrTPI (Fig. 6b and d). Increased stabilization of the nitrosyl group and limited accessibility of Cys14-SNO, which is located at the dimer interface, may further explain the presence of the nitrosothiol in the crystal structure of CrTPI exposed to GSNO.

3.7. Molecular basis for CrTPI regulation by S-nitrosylation

A characteristic feature of the TPI enzyme is the presence of four conserved catalytic residues, namely Asn11, Lys13, His95, and Glu167 (CrTPI numbering; Fig. 1). Although these residues are distantly located in the primary sequence of CrTPI (Fig. 1a), they are structurally located at a maximum distance of about 5 Å (Fig. 7a). None of these residues contains redox -sensitive side chains, suggesting that GSNO-mediated inhibition of CrTPI activity arises from structural effects induced by other residues, particularly Cys219. As already mentioned, it was reported that human TPI is *S*-nitrosylated by GSNO at Cys217 (corresponding to Cys219 in CrTPI) (Romero et al., 2018). Although this cysteine residue is located at approximately 20 Å from the active site, the partial GSNO-dependent inhibition (~30 % decrease of maximal velocity) of HsTPI was hypothesized to be dependent on long-range structural interactions between the modified amino acid and two glycines (Gly232 and Gly233 in HsTPI) (Fig. 7b). These two residues are involved in the stabilization of the phosphate group of the substrate DHAP (Noble et al., 1991), and belong to a helix-turn-helix motif harboring Ile243 (Fig. 7b). The main chain amide nitrogen of Ile243 is located at a suitable distance to allow hydrogen bonding with the nitrosyl group of Cys219. Therefore, the interaction between *S*-nitrosylated Cys219 and Ile243 could result in a conformational change in the position of the two glycines resulting in a decrease in both substrate stabilization and enzymatic catalysis. In CrTPI, Cys219 is the primary target of GSNO-dependent inhibition of enzyme activity, and the two glycines and the isoleucine are conserved (Gly234, Gly235, and Ile246 in CrTPI; Fig. 1a and Fig. 7a), supporting a similar allosteric mechanism of redox regulation for the algal enzyme. Interestingly, CrTPI and HsTPI exhibit similar extents of GSNO-dependent inhibition (~40 % and ~30 %, respectively), further supporting a conserved mode of regulation (Fig. 5). Additional studies will be needed to fully delineate the molecular pathway connecting Cys219 modification to altered catalysis in CrTPI.

4. Conclusion

Numerous studies have highlighted that plant TPI is a target of *S*-nitrosylation (Lindermayr et al., 2005; Tanou et al., 2009; Lin et al., 2012; Tanou et al., 2012; Morisse et al., 2014b; Hu et al., 2015), suggesting that this redox modification may constitute a regulatory mechanism of enzyme activity under specific physiological or stress-related circumstances. Since GSNO is the principal *S*-nitrosylating agent, we aimed to elucidate the molecular mechanisms underlying GSNO-dependent *S*-nitrosylation and to identify the regulatory Cys site (s) responsible for GSNO-dependent oxidation of TPI from the model green alga *Chlamydomonas reinhardtii*. This microalga has been widely exploited as model organism to better understand how thiol-based redox modifications (*e.g.*, *S*-nitrosylation) can modulate the activity of metabolic enzymes, but the potential impact of redox regulation on the Calvin-Benson cycle is still limited.

In this work, we exploited molecular modelling coupled with biochemical assays to demonstrate that GSNO-dependent modulation of CrTPI activity occurs through redox alteration of Cys219, although *S*-nitrosylation of this residue was not observed in the crystal of CrTPI exposed to GSNO probably for the constrains of the crystal packing (Figure S2). Conversely, Cys14 undergoes *S*-nitrosylation as revealed by structural data, but its removal does not prevent GSNO-induced inhibition.

Our experimental results evidenced that CrTPI shares with HsTPI the *S*-nitrosylation site (Cys219 in CrTPI corresponding to Cys217 in HsTPI) along with a network of residues potentially mediating redox-induced conformational changes, which supports the hypothesis that GSNO-dependent modulation of TPI activity is a conserved mechanism. This would enable modulation of TPI-dependent metabolic pathways in both human cells and microalgae under stress conditions. We further hypothesize that GSNO-dependent thiol switching of algal TPI may extend beyond the simple modulation of its catalytic activity, integrating redox signals into both glycolysis and carbon fixation. Indeed, TPI catalyzes the interconversion of G3P and DHAP with high efficiency and maintaining the equilibrium of these two sugar phosphates is critical for proper carbon allocation towards pyruvate formation in glycolysis and ribulose-1,5-bisphosphate regeneration in the carbon fixation pathway. Therefore, modulation of TPI activity may act both as a sensor and an effector of cellular redox balance, orchestrating adaptive responses to oxidative stress and metabolic fluctuations. Finally, the redox sensitivity of CrTPI could also involve other types of thiol-based post-translational modifications, including S-glutathionylation, sulfenylation, and irreversible oxidation to sulfinic and sulfonic acids. This would add a layer of complexity to its regulatory mechanisms and offer new insights into the dynamic nature of cellular metabolism in response to altered redox homeostasis. Whether such thiol-switching mechanisms (*i.e.*, *S*-nitrosylation and other redox modifications) regulate TPI enzymes in other organisms remains an open question. In this context, we speculate that the partial conservation of Cys219 (CrTPI numbering) in TPI isoforms from plant and non-plant organisms is instrumental in allowing redox modulation of these enzymes, although the involvement of other cysteines cannot be excluded.

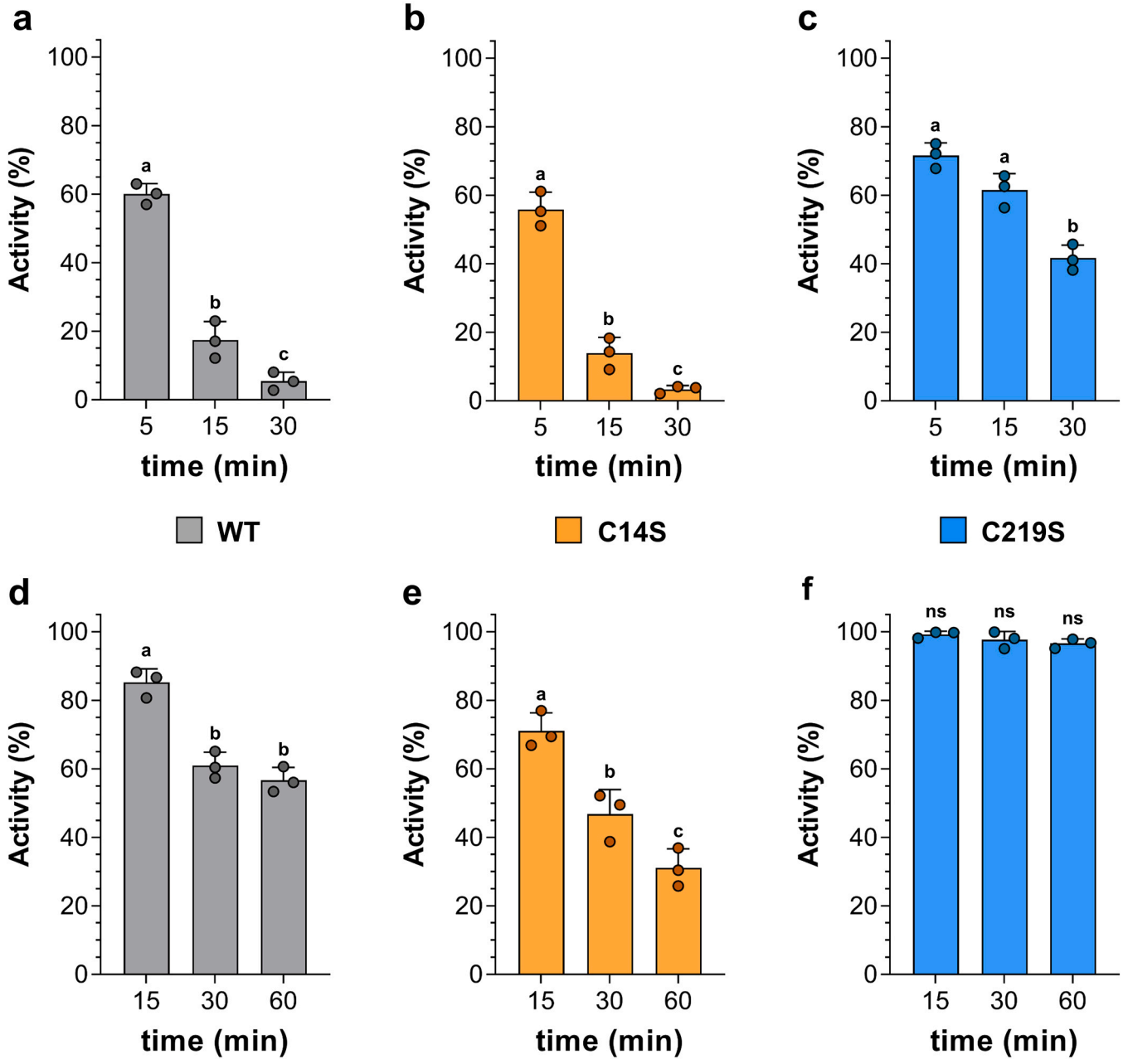

Fig. 5. Determination of redox sensitivity of CrTPI WT and Cys mutants after treatment with DTNB and GSNO. Inactivation treatments of CrTPI WT **(a)**, C14S **(b)**, and C219S **(c)** with 0.2 mM DTNB (see "Material and Methods" for further details). Data are represented as mean ± SD (n = 3). Inactivation treatments of CrTPI WT **(d)**, C14S **(e)**, and C219S **(f)** with 1 mM GSNO (see "Material and Methods" for further details). For all panels, control activity measured at each time point was set to 100 % (see Fig. 4 for specific activities of CrTPI forms) and used to calculate the percentage of residual TPI activity after incubation with 0.2 mM DTNB or 1 mM GSNO. Statistical analysis was performed as described in "Material and Methods". For each panel, letters indicate statistical differences between conditions ($P < 0.05$, ns: not significant; condition 1: residual activity compared to control activity at each time points, and condition 2: residual activities at different time points). Statistical differences between residual activities of WT with Cys variants (C14S and C219S) at each time points (15, 30, or 60 min) are provided as *P*-values in Fig. S5.

Table 1
Per-residue decomposition analysis of unmodified/*S*-nitrosylated Cys14 and Cys219 of CrTPI.

Residue	Binding energy (kcal mol^{-1})
Cys14-SH	−39.7
Cys14-SNO	−45.6
Cys219-SH	−26.8
Cys219-SNO	−28.8

CRediT authorship contribution statement

Maria Meloni: Writing – review & editing, Methodology, Investigation. **Simona Fermani:** Writing – original draft, Supervision, Investigation, Data curation, Conceptualization. **Matteo Calvaresi:** Writing – review & editing, Writing – original draft, Supervision, Methodology, Investigation, Data curation, Conceptualization. **Silvia Fanti:** Writing – review & editing, Investigation. **Edoardo Jun Mattioli:** Writing – review & editing, Methodology, Investigation. **Mirko Zaffagnini:** Writing – review & editing, Writing – original draft, Supervision, Formal

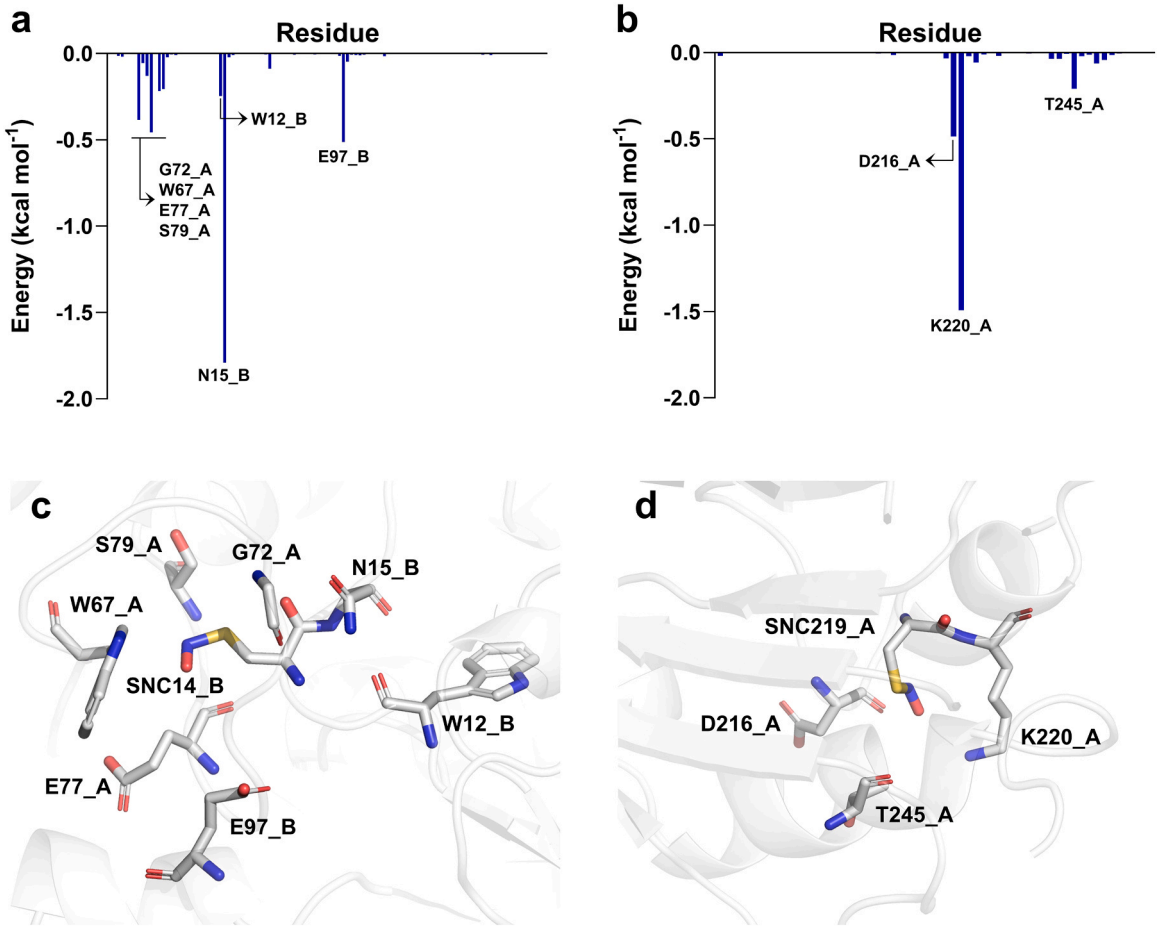

Fig. 6. Structural interactions of Cys14-SNO and Cys219-SNO in CrTPI. Binding energy ($\Delta G_{binding}$) for decomposition per CrTPI residue of Cys14-SNO **(a)** and Cys219-SNO **(b)**. Structural snapshot of the interactions mediated by hydrogen bonds of Cys14-SNO (SNC14_B) **(c)** and Cys219 (SNC219_A) **(d)** with surrounding residues.

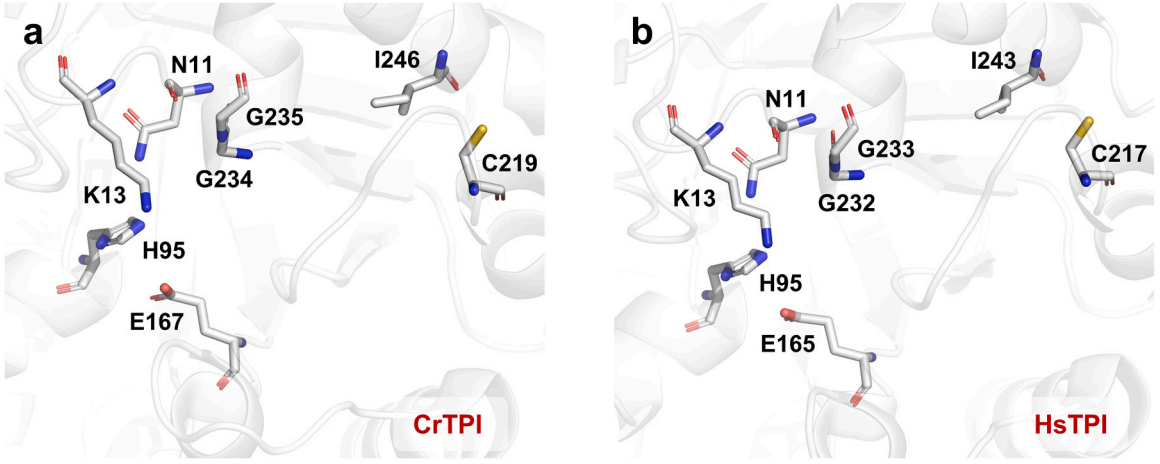

Fig. 7. Representation of the active site of CrTPI (a) and HsTPI (b). In both panels, the four catalytic residues and residues potentially involved in the enzymatic modulation mediated by *S*-nitrosylation of Cys219 in CrTPI and Cys217 in HsTPI are shown.

analysis, Data curation, Conceptualization. **Julien Henri:** Writing – review & editing, Investigation. **Daniele Tedesco:** Writing – review & editing, Investigation. **Stéphane D. Lemaire:** Writing – review & editing. **Paolo Trost:** Writing – review & editing. **Ginevra Marie Eloise Peppi:** Writing – review & editing, Investigation. **Giuseppe Gabellini:** Writing – review & editing, Investigation. **Tancredi Bin:** Writing – review & editing, Investigation.

Funding

This research did not receive any specific grant from funding agencies in the public, commercial, or not-for-profit sectors.

Declaration of Competing Interest

The authors declare that they have no known competing financial interests or personal relationships that could have appeared to influence the work reported in this paper.

Acknowledgements

MZ is indebted to Dr. Anfisa Letyago and Dr. Layla Benitez for stimulating advices and discussion. E.J.M. was supported by Fondazione Umberto Veronesi. GMEP is supported by a PhD grant financed by European Union - Next Generation EU, Mission 4, Investment 4.1 (D.M. 118/2023) CUP J33C23002510002 (PhD program in Cellular and Molecular Biology, University of Bologna, Italy). We gratefully acknowledge Diamond Light Source (Oxfordshire, UK) and the European Synchrotron Radiation Facility (ESRF, Grenoble, France) for allocation of beam time (BAG proposals MX21741 and MX2291, respectively) and the staff of beamlines I03 at Diamond and ID30A-2 at ESRF for technical support.

Appendix A. Supporting information

Supplementary data associated with this article can be found in the online version at doi:10.1016/j.plantsci.2025.112768.

Data availability

Data will be made available on request.

References

P.D. Adams, P.V. Afonine, G. Bunkoczi, V.B. Chen, I.W. Davis, N. Echols, J.J. Headd, L. W. Hung, G.J. Kapral, R.W. Grosse-Kunstleve, A.J. McCoy, N.W. Moriarty, R. Oeffner, R.J. Read, D.C. Richardson, J.S. Richardson, T.C. Terwilliger, P.H. Zwart, PHENIX: a comprehensive Python-based system for macromolecular structure solution, Acta Crystallogr D. Biol. Crystallogr. 66 (2010) 213–221.

R. Anandakrishnan, B. Aguilar, A.V. Onufriev, H++ 3.0: automating pk prediction and the preparation of biomolecular structures for atomistic molecular modeling and simulations, Nucleic Acids Res. 40 (2012) W537–541.

D.W. Banner, A.C. Bloomer, G.A. Petsko, D.C. Phillips, C.I. Pogson, I.A. Wilson, P. H. Corran, A.J. Furth, J.D. Milman, R.E. Offord, J.D. Priddle, S.G. Waley, Structure of chicken muscle triose phosphate isomerase determined crystallographically at 2.5 angstrom resolution using amino acid sequence data, Nature 255 (1975) 609–614.

D.A. Case, T.E. Cheatham 3rd, T. Darden, H. Gohlke, R. Luo, K.M. Merz Jr., A. Onufriev, C. Simmerling, B. Wang, R.J. Woods, The amber biomolecular simulation programs, J. Comput. Chem. 26 (2005) 1668–1688.

X. Chen, D. Tian, X. Kong, Q. Chen, F.A. E, X. Hu, A. Jia, The role of nitric oxide signalling in response to salt stress in chlamydomonas reinhardtii, Planta 244 (2016) 651–669.

P. Emsley, K. Cowtan, Coot: model-building tools for molecular graphics, Acta Crystallogr D. Biol. Crystallogr. 60 (2004) 2126–2132.

P. Evans, Scaling and assessment of data quality, Acta Crystallogr D. Biol. Crystallogr. 62 (2006) 72–82.

P.R. Evans, G.N. Murshudov, How good are my data and what is the resolution? Acta Crystallogr D. Biol. Crystallogr. 69 (2013) 1204–1214.

M.W. Foster, D.T. Hess, J.S. Stamler, Protein S-nitrosylation in health and disease: a current perspective, Trends Mol. Med. 15 (2009) 391–404.

R.J. Gildea, J. Beilsten-Edmands, D. Axford, S. Horrell, P. Aller, J. Sandy, J. Sanchez-Weatherby, C.D. Owen, P. Lukacik, C. Strain-Damerell, R.L. Owen, M.A. Walsh, G. Winter, xia2.multiplex: a multi-crystal data-analysis pipeline, Acta Crystallogr. D. Struct. Biol. 78 (2022) 752–769.

P. Gouet, E. Courcelle, D.I. Stuart, F. Metoz, ESPript: analysis of multiple sequence alignments in PostScript, Bioinformatics 15 (1999) 305–308.

S. Han, Force field parameters for S-nitrosocysteine and molecular dynamics simulations of S-nitrosated thioredoxin, Biochem Biophys. Res Commun. 377 (2008) 612–616.

J.R. Helliwell, Triosephosphate isomerase: the perfect enzyme, but how does it work? IUCrJ 8 (2021) 480–481.

D.T. Hess, A. Matsumoto, S.O. Kim, H.E. Marshall, J.S. Stamler, Protein S-nitrosylation: purview and parameters, Nat. Rev. Mol. Cell Biol. 6 (2005) 150–166.

J. Hu, X. Huang, L. Chen, X. Sun, C. Lu, L. Zhang, Y. Wang, J. Zuo, Site-specific nitrosoproteomic identification of endogenously S-nitrosylated proteins in arabidopsis, Plant Physiol. 167 (2015) 1731–1746.

X. Johnson, J. Alric, Central carbon metabolism and electron transport in chlamydomonas reinhardtii: metabolic constraints for carbon partitioning between oil and starch, Eukaryot. Cell 12 (2013) 776–793.

P.A. Kollman, I. Massova, C. Reyes, B. Kuhn, S. Huo, L. Chong, M. Lee, T. Lee, Y. Duan, W. Wang, O. Donini, P. Cieplak, J. Srinivasan, D.A. Case, T.E. Cheatham 3rd, Calculating structures and free energies of complex molecules: combining molecular mechanics and continuum models, Acc. Chem. Res 33 (2000) 889–897.

D. Liebschner, P.V. Afonine, M.L. Baker, G. Bunkoczi, V.B. Chen, T.I. Croll, B. Hintze, L. W. Hung, S. Jain, A.J. McCoy, N.W. Moriarty, R.D. Oeffner, B.K. Poon, M.G. Prisant, R.J. Read, J.S. Richardson, D.C. Richardson, M.D. Sammito, O.V. Sobolev, D. H. Stockwell, T.C. Terwilliger, A.G. Urzhumtsev, L.L. Videau, C.J. Williams, P. D. Adams, Macromolecular structure determination using X-rays, neutrons and electrons: recent developments in phenix, Acta Crystallogr D. Struct. Biol. 75 (2019) 861–877.

A. Lin, Y. Wang, J. Tang, P. Xue, C. Li, L. Liu, B. Hu, F. Yang, G.J. Loake, C. Chu, Nitric oxide and protein S-nitrosylation are integral to hydrogen peroxide-induced leaf cell death in rice, Plant Physiol. 158 (2012) 451–464.

C. Lindermayr, G. Saalbach, J. Durner, Proteomic identification of S-nitrosylated proteins in arabidopsis, Plant Physiol. 137 (2005) 921–930.

L.M. Lopez-Castillo, P. Jimenez-Sandoval, N. Baruch-Torres, C.H. Trasvina-Arenas, C. Diaz-Quezada, S. Lara-Gonzalez, R. Winkler, L.G. Brieba, Structural basis for redox regulation of cytoplasmic and chloroplastic triosephosphate isomerases from arabidopsis thaliana, Front Plant Sci. 7 (2016) 1817.

J.A. Maier, C. Martinez, K. Kasavajhala, L. Wickstrom, K.E. Hauser, C. Simmerling, ff14SB: improving the accuracy of protein side chain and backbone parameters from ff99SB, J. Chem. Theory Comput. 11 (2015) 3696–3713.

E.J. Mattioli, J. Rossi, M. Meloni, M. De Mia, C.H. Marchand, A. Tagliani, S. Fanti, G. Falini, P. Trost, S.D. Lemaire, S. Fermani, M. Calvaresi, M. Zaffagnini, Structural snapshots of nitrosoglutathione binding and reactivity underlying S-nitrosylation of photosynthetic GAPDH, Redox Biol. 54 (2022) 102387.

A.J. McCoy, R.W. Grosse-Kunstleve, P.D. Adams, M.D. Winn, L.C. Storoni, R.J. Read, Phaser crystallographic software, J. Appl. Crystallogr. 40 (2007) 658–674.

M. Meloni, S. Fanti, D. Tedesco, L. Gurrieri, P. Trost, S. Fermani, S.D. Lemaire, M. Zaffagnini, J. Henri, Characterization of chloroplast ribulose-5-phosphate-3-epimerase from the microalga chlamydomonas reinhardtii, Plant Physiol. 194 (2024a) 2263–2277.

M. Meloni, J. Rossi, S. Fanti, G. Carloni, D. Tedesco, P. Treffon, L. Piccinini, G. Falini, P. Trost, E. Vierling, F. Licausi, B. Giuntoli, F. Musiani, S. Fermani, M. Zaffagnini, Structural and biochemical characterization of arabidopsis alcohol dehydrogenases reveals distinct functional properties but similar redox sensitivity, Plant J. 118 (2024b) 1054–1070.

L. Michelet, M. Zaffagnini, S. Morisse, F. Sparla, M.E. Pérez-Pérez, F. Francia, A. Danon, C.H. Marchand, S. Fermani, P. Trost, S.D. Lemaire, Redox regulation of the Calvin-Benson cycle: something old, something new, Front. Plant Sci. 4 (2013) 470.

S. Morisse, L. Michelet, M. Bedhomme, C.H. Marchand, M. Calvaresi, P. Trost, S. Fermani, M. Zaffagnini, S.D. Lemaire, Thioredoxin-dependent redox regulation of chloroplastic phosphoglycerate kinase from chlamydomonas reinhardtii, J. Biol. Chem. 289 (2014a) 30012–30024.

S. Morisse, M. Zaffagnini, X.H. Gao, S.D. Lemaire, C.H. Marchand, Insight into protein S-nitrosylation in chlamydomonas reinhardtii, Antioxid. Redox Signal 21 (2014b) 1271–1284.

G.N. Murshudov, A.A. Vagin, E.J. Dodson, Refinement of macromolecular structures by the maximum-likelihood method, Acta Crystallogr D. Biol. Crystallogr. 53 (1997) 240–255.

M.E. Noble, R.K. Wierenga, A.M. Lambeir, F.R. Opperdoes, A.M. Thunnissen, K.H. Kalk, H. Groendijk, W.G. Hol, The adaptability of the active site of trypanosomal triosephosphate isomerase as observed in the crystal structures of three different complexes, Proteins 10 (1991) 50–69.

C. Qiu, J. Sun, Y. Wang, L. Sun, H. Xie, Y. Ding, W. Qian, Z. Ding, First nitrosoproteomic profiling deciphers the cysteine S-nitrosylation involved in multiple metabolic pathways of tea leaves, Sci. Rep. 9 (2019) 17525.

J.M. Romero, M.E. Carrizo, J.A. Curtino, Characterization of human triosephosphate isomerase S-nitrosylation, Nitric Oxide 77 (2018) 26–34.

Q. Shi, J. Feng, H. Qu, Y.Y. Cheng, A proteomic study of S-nitrosylation in the rat cardiac proteins in vitro, Biol. Pharm. Bull. 31 (2008) 1536–1540.

F. Sievers, A. Wilm, D. Dineen, T.J. Gibson, K. Karplus, W. Li, R. Lopez, H. McWilliam, M. Remmert, J. Soding, J.D. Thompson, D.G. Higgins, Fast, scalable generation of high-quality protein multiple sequence alignments using clustal omega, Mol. Syst. Biol. 7 (2011) 539.

A. Tagliani, J. Rossi, C.H. Marchand, M. De Mia, D. Tedesco, L. Gurrieri, M. Meloni, G. Falini, P. Trost, S.D. Lemaire, S. Fermani, M. Zaffagnini, Structural and functional insights into nitrosoglutathione reductase from chlamydomonas reinhardtii, Redox Biol. 38 (2021) 101806.

G. Tanou, P. Filippou, M. Belghazi, D. Job, G. Diamantidis, V. Fotopoulos, A. Molassiotis, Oxidative and nitrosative-based signaling and associated post-translational modifications orchestrate the acclimation of citrus plants to salinity stress, Plant J. 72 (2012) 585–599.

G. Tanou, C. Job, L. Rajjou, E. Arc, M. Belghazi, G. Diamantidis, A. Molassiotis, D. Job, Proteomics reveals the overlapping roles of hydrogen peroxide and nitric oxide in the acclimation of citrus plants to salinity, Plant J. 60 (2009) 795–804.

P. Treffon, J. Rossi, G. Gabellini, P. Trost, M. Zaffagnini, E. Vierling, Quantitative proteome profiling of a S-Nitrosoglutathione reductase (GSNOR) null mutant reveals a new class of enzymes involved in nitric oxide homeostasis in plants, Front Plant Sci. 12 (2021) 787435.

O. Trott, A.J. Olson, AutoDock vina: improving the speed and accuracy of docking with a new scoring function, efficient optimization, and multithreading, J. Comput. Chem. 31 (2010) 455–461.

C. Vonrhein, C. Flensburg, P. Keller, A. Sharff, O. Smart, W. Paciorek, T. Womack, G. Bricogne, Data processing and analysis with the autoPROC toolbox, Acta Crystallogr D. Biol. Crystallogr 67 (2011) 293–302.

R.K. Wierenga, E.G. Kapetaniou, R. Venkatesan, Triosephosphate isomerase: a highly evolved biocatalyst, Cell Mol. Life Sci. 67 (2010) 3961–3982.
M.D. Winn, C.C. Ballard, K.D. Cowtan, E.J. Dodson, P. Emsley, P.R. Evans, R.M. Keegan, E.B. Krissinel, A.G. Leslie, A. McCoy, S.J. McNicholas, G.N. Murshudov, N.S. Pannu, E.A. Potterton, H.R. Powell, R.J. Read, A. Vagin, K.S. Wilson, Overview of the CCP4 suite and current developments, Acta Crystallogr D. Biol. Crystallogr 67 (2011) 235–242.
M. Zaffagnini, M. Bedhomme, C.H. Marchand, S. Morisse, P. Trost, S.D. Lemaire, Redox regulation in photosynthetic organisms: focus on glutathionylation, Antioxid. Redox Signal 16 (2012) 567–586.
M. Zaffagnini, M. De Mia, S. Morisse, N. Di Giacinto, C.H. Marchand, A. Maes, S. D. Lemaire, P. Trost, Protein S-nitrosylation in photosynthetic organisms: a comprehensive overview with future perspectives, Biochim. Biophys. Acta 1864 (2016) 952–966.
M. Zaffagnini, S. Fermani, C.H. Marchand, A. Costa, F. Sparla, N. Rouhier, P. Geigenberger, S.D. Lemaire, P. Trost, Redox homeostasis in photosynthetic organisms: novel and established Thiol-Based molecular mechanisms, Antioxid. Redox Signal 31 (2019a) 155–210.
M. Zaffagnini, C.H. Marchand, M. Malferrari, S. Murail, S. Bonacchi, D. Genovese, M. Montalti, G. Venturoli, G. Falini, M. Baaden, S.D. Lemaire, S. Fermani, P. Trost, Glutathionylation primes soluble glyceraldehyde-3-phosphate dehydrogenase for late collapse into insoluble aggregates, Proc. Natl. Acad. Sci. USA 116 (2019b) 26057–26065.
M. Zaffagnini, L. Michelet, C. Sciabolini, N. Di Giacinto, S. Morisse, C.H. Marchand, P. Trost, S. Fermani, S.D. Lemaire, High-resolution crystal structure and redox properties of chloroplastic triosephosphate isomerase from chlamydomonas reinhardtii, Mol. Plant 7 (2014) 101–120.
S. Zahid, R. Khan, M. Oellerich, N. Ahmed, A.R. Asif, Differential S-nitrosylation of proteins in alzheimer's disease, Neuroscience 256 (2014) 126–136.